

Graphene-Based Supercapacitor Using Microemulsion Electrolyte

Aliyu Salisu,^[b] Fraser Hughson,^[c] Rohan Borah,^[c] Xianjue Chen,^[b] Anish Johns,^[a] Alex Griesser,^[d] Gunther G. Andersson,^[d] Thomas Nann,*^[c] and Renee V. Goreham*^[a]

Graphene-like material prepared by a facile combustion synthesis was investigated as an electrode material in a microemulsion electrolyte. Notably, a stable voltage window of 2.2–2.4 V was achieved, surpassing previous reports for aqueous-based electrolytes on similar materials. The fabricated supercapacitor device exhibited a commendable specific capacitance values of 59 F g^{-1} at 0.1 A g^{-1} and 32 F g^{-1} at 5 A g^{-1} , indicating its potential for high-current applications. Mechanistic examination revealed that the charge storage primarily relies on electric double-layer formation, with minor non-capacitive contribution

from electrode surface functionalities and the supporting electrolyte. Further analysis showed significant capacitive contributions of 85% at 2.2 V and 67% at 2.4 V, underscoring the dominance of the capacitive process. The fabricated supercapacitor's stability indicated a decrease as the non-capacitive process intensified, suggesting that electrode surface functionalities predominantly contribute to cell deterioration at elevated potentials. These results highlight the potential efficacy of microemulsion electrolytes in energy storage applications.

Introduction

Supercapacitors, also known as electrochemical double-layer capacitors (EDLC), are energy storage devices renowned for their exceptional power output, fast charging and discharging process, long cycle life, and safe operation properties.^[1–6] They outperform batteries across numerous metrics except in their energy density, which to date, remains their main drawback. Their energy density is primarily determined by the electrode's capacitance and the voltage window of the electrolyte, i.e. the potential range within which the electrolyte is stable. Consequently, optimizing the selection of electrodes and electrolytes holds the ability to enhance their overall energy density.^[7]

In the context of supercapacitor development, various electrode materials have been explored, with graphene-like materials (or chemically modified graphene) emerging as the most promising candidate owing to their exceptional theoretical surface area (potentially up to $2630 \text{ m}^2 \text{ g}^{-1}$), high electrical conductivity, as well as robust electrochemical stability.^[8,9] Several studies have highlighted the unique performance

characteristics of these materials in supercapacitors.^[9,10] For instance, Ruoff et al. achieved a specific capacitances of 135 F g^{-1} and 99 F g^{-1} in aqueous and organic electrolytes, respectively.^[11] Graphene-based electrodes in ionic liquids exhibited a specific capacitance in the range of $75\text{--}90 \text{ F g}^{-1}$.^[12,13]

Regarding the electrolytic materials for supercapacitors, current options include organic solvents, ionic liquids, and aqueous electrolytes.^[14] Organic and ionic liquids electrolytes, despite offering a high voltage window (2.5–3.5 V), have raised environmental concerns and suffer from obvious limitations such as prohibitive cost, toxicity, and low ionic conductivities.^[14] In contrast, aqueous electrolytes exhibit high conductivity, possess eco-friendly characteristics and they are low cost. However, their voltage window is generally restricted to 1.23 V due to the thermodynamically favoured water-splitting reaction that occurs beyond this limit.^[14–17] Consequently, aqueous-based supercapacitors are preferable for applications that require a low voltage ($\sim 1 \text{ V}$) to prevent performance degradation and undesired reactions. Notably, some studies have extended the voltage window of aqueous electrolytes to 1.6–2.0 V in neutral alkali sulfate solutions, attributing the overpotential to the absorption of hydrogen into the electrode, and the fact that the dehydration energy of ions at neutral pH does not favor water splitting at low potentials.^[16–18]

Microemulsions (MEs)-based electrolytes are innovative electrolytes recently proposed for energy storage applications. They are a thermodynamically stable, isotropic dispersion comprising of immiscible liquids stabilized by a surfactant.^[19–21] MEs-based electrolytes uniquely combine the high conductivity of aqueous electrolytes with the wide electrochemical window of organic electrolytes, which are essential for high-performance energy storage devices.

Historically, numerous studies have examined the use of MEs as media for electroanalytical studies and electrochemical reactions, thanks to their unique solubilization properties and

[a] A. Johns, Dr. R. V. Goreham
School of Information and Physical Sciences, University of Newcastle, Callaghan, NSW, 2308, Australia
E-mail: Renee.goreham@newcastle.edu.au

[b] A. Salisu, Dr. X. Chen
School of Environmental and Life Sciences, University of Newcastle, Callaghan, NSW, 2308, Australia

[c] Dr. F. Hughson, Dr. R. Borah, Prof. T. Nann
Allegro Energy Pty Ltd, Thornton, 2232, Australia
E-mail: Thomas@allegro.energy

[d] A. Griesser, Prof. G. G. Andersson
Flinders Institute for Nanoscale Science and Technology, Flinders University, Adelaide, South Australia 5042, Australia

 Supporting information for this article is available on the WWW under <https://doi.org/10.1002/batt.202400305>

diverse characteristics across different phases.^[21–28] There are also some significant reports detailing the diffusion and electron transfer process between electrochemical probes and electrodes in MEs.^[24,29–31] Recent research highlights their effectiveness in redox flow batteries (RFBs) due to their ability to decouple ionic conductivity and the solubility of redox-active molecules, presenting a promising alternative for enhancing the energy density and conductivity of redox species.^[31–36] For instance, Shuting and colleagues developed a stable ME RFB using 2-methyl anthraquinone and ferrocene, achieving a coulombic efficiency (CE) of 96%, a voltage efficiency (VE) of 80%, and an energy efficiency (EE) of 76.6% after 300 cycles, indicating high stability and efficiency compared to other MEs-based RFBs.^[33]

Despite the significant progress in using MEs in electrochemistry, their application in supercapacitor has been scarcely reported, with only two notable studies.^[37,38] Our research group was first to demonstrate high performance of sodium dodecyl sulfate (SDS) based ME in supercapacitor.^[37] Notably, we achieved high voltage window (2.7 V), surpassing the typical 1.23 V barrier observed in aqueous electrolytes, despite water being the major component of the ME. Utilizing an activated carbon electrode, we attained a specific capacitance of 40 F g^{-1} , with 99% capacitance retention after 10,000 cycles. Most recently, Liu and Peng reported an enhanced voltage window (2.9 V) using ME formulated with tween 20 surfactant.^[38] The authors showed high capacitance retention (86.62–100%) after 4000 cycles at different current rate (1–3 mA cm^{-2}). However, the high internal resistance caused by ion movement lag in the electrolytes has raised concerns.

It is noteworthy that both reports suggested that the extended voltage window in MEs in supercapacitor, results from the formation of a hydrophobe-dominant region perpendicular to the electrode surface, which restricts water interaction and suppresses water splitting, thus enabling a larger voltage window. Notably, the reported voltage window in both studies were measured on a glassy carbon surface (GC), known to have a high overpotential to water splitting.^[39] Therefore, the voltage window may vary with different electrodes, such as graphene or activated carbon electrodes, necessitating a more realistic analysis.

We have, for the first time, investigated the electrochemical performance of SDS-based ME on a graphene-based electrode in a symmetrical supercapacitor. Additionally, we explored the cell stability and analyzed the pseudo-capacitive contribution from the electrolyte and electrode surface functionalities. An SDS-based ME was chosen for its low viscosity, good conductivity, availability, and sustainable characteristics, offering promising avenues for advanced energy storage systems.^[37]

Results and Discussion

The decomposition (or “reduction”) of graphene oxide (G–O) has been widely used for producing graphene-like materials, with properties approaching those of graphene; a two-dimensional, single layer sheet of sp^2 hybridized carbon atoms.

Several reduction techniques have been explored in the literature, with thermal (high temperature treatment) and chemical (such as the hydrazine hydrate approach) reduction routes being the most prevalent.^[9,40,41] In this paper, a straightforward combustion synthesis method using a mixture of urea and ammonium nitrate was employed for the conversion of G–O to a reduce graphene oxide (r-GO).^[42]

Within the mixture, the urea acts as a fuel while the ammonium nitrate is an oxidizer, leading to an exothermic reaction that increases the temperature of the reaction. In contrast to the thermal reduction method, which utilizes elevated exfoliation temperatures, the combustion process is limited to a temperature of 250 °C for exfoliation. This is because urea reacts with ammonium nitrate at 230 °C, resulting in a rapid generation of heat via an exothermic reaction which facilitates the thermal removal of oxygen from G–O, and promotes the exfoliation of G–O to r-GO through the release of gases. This process has been demonstrated via thermogravimetric analysis and differential scanning calorimetry profiles.^[42,43]

To characterize the microtexture of the synthesized r-GO, nitrogen adsorption/desorption isotherms were measured. The adsorption curve exhibited the typical pattern of a type II isotherm, featuring a hysteresis loop within the range of 0.5–1 p/p₀, indicative of mesoporous characteristics of porous like materials (Figure 1(a)). The pore size distribution computed using 2D-NLDFT method, showed a distribution of mesopores, ranging from 4 to 13 nm (inset of Figure 1(a)). Brunauer-Emmet-Teller (BET) measurement indicated a rise in the specific surface area from $35 \text{ m}^2 \text{ g}^{-1}$ (for G–O) to $522 \text{ m}^2 \text{ g}^{-1}$ (for r-GO).

Figure 1(b) depicts a typical image of the r-GO as obtained through transmission electron microscopy (TEM). The TEM image illustrates the presence of graphene-like thin sheets that are readily accessible to electrolytes. The sheets exhibit a wrinkled appearance, attributed to the presence of structural defects, notably oxygenated and nitrogenated functionalities. Raman spectral analysis of the r-GO (Figure 1(c)) reveals an increase in the intensity ratio of the “D” and “G” bands (I_D/I_G) at approximately 1354 cm^{-1} and 1598 cm^{-1} , rising from 0.89 for G–O to 1.06 for the r-GO. A broader and more intense D band typically occurs where carbon edge defects and structural disorders are present after the thermal decomposition and exfoliation.^[44] Elemental composition analysis revealed approximately 12.5% oxygen and 11% of nitrogen contents within the r-GO sample.

X-ray photoelectron spectroscopic (XPS) analysis performed on the r-GO is shown in Figure 1(d). In the C1s XPS spectrum, the predominant peak observed at 284.5 eV signifies the presence of sp^2 hybridized carbon atoms. Additionally, smaller peaks at 285–291 eV are characteristics of sp^3 hybridized carbon atoms and other functional groups such as carboxyl ($\text{O}-\text{C}=\text{O}$), carbonyl ($-\text{C}=\text{O}$), and carbonate ($\text{O}-\text{C}(=\text{O})-\text{O}$). The distribution analysis of the carbon atoms (Figure S1) reveals that approximately 70% of the carbon atoms are associated with the graphite sp^2 carbon, at 284.5 eV. This indicates a reduced presence of surface functional groups in the r-GO compared to G–O (Figure S2a), illustrating a considerable degree of reduc-

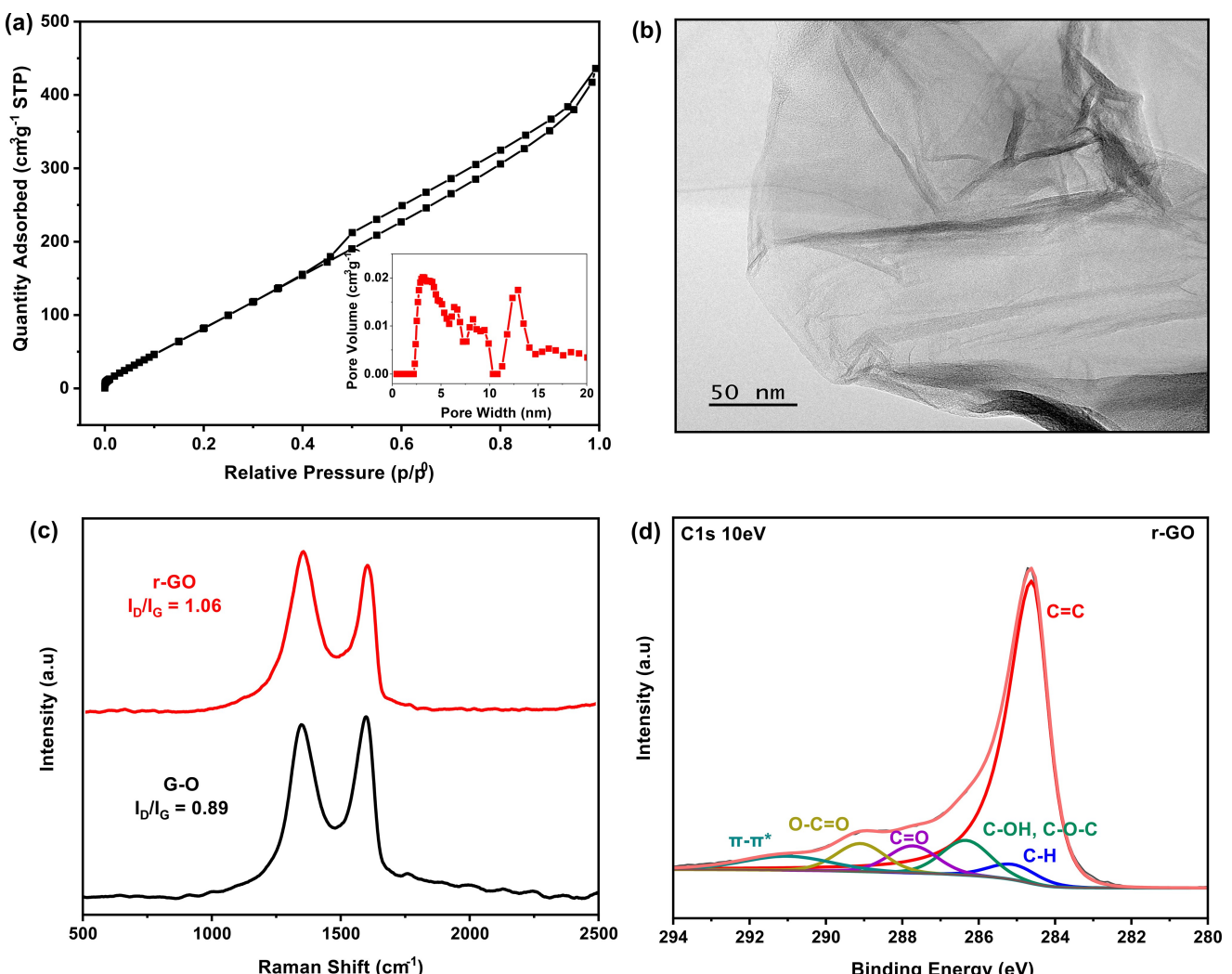


Figure 1. (a) Nitrogen adsorption/desorption isotherm and pore size distribution (Inset) calculated by 2D-NLDFT method. (b) TEM image of the as-prepared r-GO at 50 nm resolution. (c) Raman spectra of G-O and r-GO. (d) XPS C1s spectrum of r-GO showing the removal of the oxygen-containing groups.

tion. The N1s spectrum of the r-GO (Figure S2b) exhibits a prominent peak at 399.69 eV, representing roughly 76.6% of the nitrogen distribution. This peak is attributed to pyrrolic nitrogen functionality. The presence of nitrogen-containing group in the r-GO suggests that during the combustion process, a significant amount of nitrogen from the urea/ammonium nitrate mixture was doped, leading to the modification of the physical and chemical properties of the r-GO. Significant studies have pointed out the effect of N-doping in supercapacitor performance enhancement, primarily due to its pseudocapacitive contribution.^[9,45]

In contrast, the N1s spectrum of G-O reveals no presence of nitrogen-containing groups, indicating that the doping took place during the combustion process. Furthermore, the G-O C1s spectrum (Figure S2a) showed an intense peak at 285–291 eV region, suggesting a high degree of oxidation and consequently, more surface functionalities. A notable observation in the XPS result is a substantial decrease in the O/C ratio from 0.38 for G-O to 0.16 for r-GO. This data suggests a substantial removal of oxygen from the G-O during the

synthesis. A previous study showed that the combustion of G-O reduces carbonyl and carboxyl bonds to a greater extent.^[42]

The electrochemical performance of both r-GO and G-O was studied in novel high-voltage ME-based electrolyte. Initially, Cyclic Voltammetry (CV) measurements were performed at 20 mVs^{-1} to investigate the operational cell voltage window of 0.1 M KCl ME on r-GO electrode.^[7] Using a three-electrode cell set-up comprising r-GO working electrode, Pt counter, and Ag/AgCl reference electrode, the positive and negative limits of a single electrode versus Ag/AgCl were determined. Figure S3(a) demonstrated a voltage window of approximately 2.48 V (−1.39 to 1.09 V, vs Ag/AgCl), indicating a high negative overpotential for hydrogen evolution reaction. The high overpotential is attributed to the storage of nascent hydrogen in r-GO below the thermodynamic potential for water splitting, as previously suggested.^[16,17] A noticeable peak at approximately 0.5–0.6 V vs Ag/AgCl during the positive scan is associated with the electro-oxidation of the stored hydrogen (Figure S3(b)).^[17] The peak and the negative current are correlated as both sharply intensify

after -1.4 V vs Ag/AgCl, indicating gas evolution and marking the limit for the negative potential. Figure S3(c) presents the Linear Sweep Voltammetry (LSV) of the cell, which corroborates the voltage window observed in the CV, confirming an apparent ME voltage window of $2.45\text{--}2.48$ V. This is significantly higher when compared to the standard aqueous electrolytes based on 0.5 M Na₂SO₄ and 6 M KOH, which showed a voltage window of 1.6 V (-1 to 0.6 V, vs Ag/AgCl) and 1.1 V (-1 to 0.1 V, vs Ag/AgCl), respectively (Figure S3d).

It is crucial to note that the observed voltage window (2.48 V vs Ag/AgCl) of the ME using a single electrode might not accurately represent the true working potential for a fully assembled supercapacitor cell. In a fully assembled cell, the voltage arises from the synergy between the positive and negative electrode surfaces. Consequently, if one of the electrodes reaches its limit before the other, it results in an overall decline in the cell performance. This in turn results to a lack of full utilization of the voltage window as compared to a single electrode setup.^[46,47] Indeed, CV measurement conducted on the full cell at various cut-off potentials ($2.0\text{--}2.5$ V) revealed a

reduction in the voltage window, decreasing from 2.48 V to approximately $2.2\text{--}2.4$ V (Figure 2(a)).

To gain more insight into the voltage window, galvanostatic charge discharge (GCD) measurements were conducted at various cut-off potentials, ranging from 2.0 to 2.5 V. GCD testing stands as the most versatile and commonly utilized technique for characterizing supercapacitors operating under direct currents.^[7] The results (Figure 2(b)) revealed a typical supercapacitor GCD curves till 2.4 V, after which the curves starts plateauing, indicating a decrease in the overall efficiencies. The decrease in the efficiency is attributed to irreversible side reactions stemming from either the electrode or from the interaction between the electrode and the electrolyte. Figure S4 illustrates the coulombic and the energy efficiencies as the function of the applied potential. Both efficiencies stand above 80% at $2.2\text{--}2.4$ V, falling within the recommended efficiency ranges. Values below 80% efficiencies may indicate instability, degradation, and potential end life of a cell.^[46,47]

Later GCD measurement using a reference electrode confirmed that the positive electrode is the limiting electrode, indicating that the voltage range of the negative electrode was

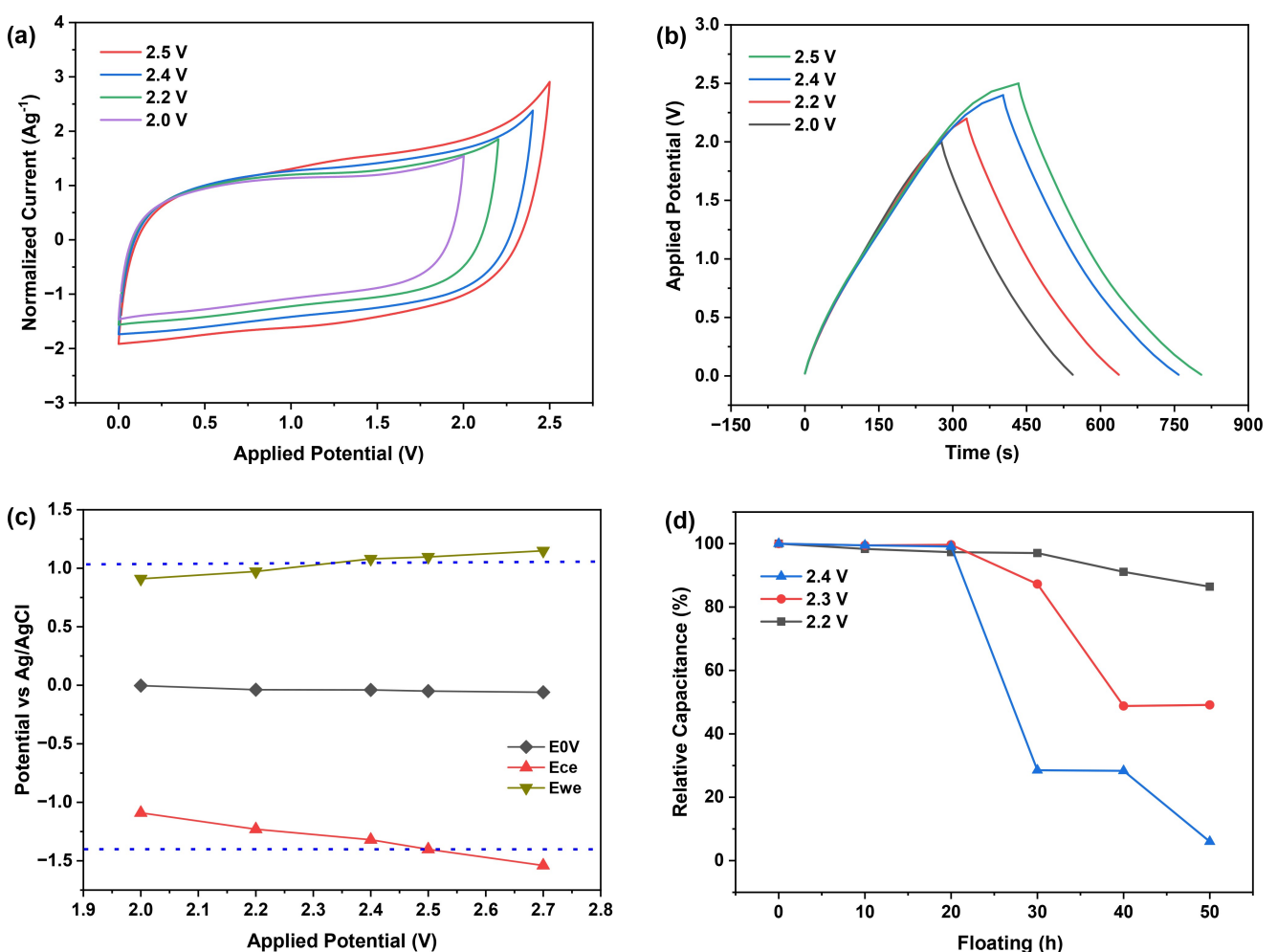


Figure 2. (a) Cyclic voltammograms at different cut-off potential at 100 mVs $^{-1}$. (b) Galvanostatic charge discharge (GCD) curves at different potentials, at 0.1 A g $^{-1}$. (c) GCD curves of r-GO in 0.1 M KCl ME, depicting positive and negative electrode potentials and the practical potential limits (dotted line) determined from CV three electrode measurements. (d) GCD floating test (r-GO in 0.1 M KCl ME at 0.1 A g $^{-1}$) versus relative capacitance.

underused. Figure 2(c) shows that the positive electrode (E_{we}) reaches its limit around 1.08 V, which correlates to a negative electrode potential (E_{ce}) of around -1.24 V, resulting in an overall operational voltage of approximately 2.32 V. Notably, this window is narrower compared to the previously reported ME voltage windows (2.5 V^[37] and 2.9 V^[38]) in supercapacitor. This is potentially due to the electrode surface functionalities/electrochemical oxidation of the electrode surface. Surface functionalities, specifically oxygenated and nitrogenated groups, are acknowledged for constraining the achievable window at high voltages. This limitation arises from surface redox reactions with the electrolytes.^[9,16] Additionally, the incorporation of heteroatoms (such as nitrogen or oxygen) into the nanostructure of an electrode surface can modify its wettability, thereby enhancing the hydrophilicity of the surface. This facilitates degradation through hydrogen evolution reaction.^[48] In this context, we suggest that the observed limitation in the window is attributed to the electrode (r-GO) rather than the ME electrolyte.

To ascertain the stability within the suggested operational window, a floating test was conducted at 2.2 V, 2.3 V, and 2.4 V. The test involved five sequential GCD cycles and a 10 h voltage holding step at 0.1 A g⁻¹ (based on the mass of two electrodes).^[49,50] Some studies have described a similar test with five GCD cycles and a 2 h holding step at a higher current rate of 1 A g⁻¹.^[51] In both cases, the capacitance values after the fifth cycle of each sequence were calculated and compared to the initial capacitance value. The results presented here are based on a 10 h voltage holding. In Figure 2(d), the capacitance retention as a function of the floating time is illustrated. Interestingly, a remarkable capacitance retention of over 85% was achieved at 2.2 V, after the floating period. Figures S5(a) and S5(b) illustrate the CV curves before and after the floating test, along with GCD curves during the floating. Both the CV and GCD measurements demonstrated characteristic supercapacitor's curves, indicating exceptional capacitance behavior and remarkable charge-discharge operation.

At a floating potential of 2.3 V, high capacitance retention values were observed in the first 20 h, above which the retention capability reduces to 87% and 50% at 30 and 50 floating h, respectively (Figure 2(d)). This result suggests the cell's capability to operate at 2.3 V, though possible surface redox activities may cause deterioration in the charge-discharge operation. However, at 2.4 V floating potential, the cell experienced over 80% initial capacitance loss after 20 h of floating (Figure 2(d)). GCD, CV and EIS measurements after the floating confirmed the cell degradation (Figures S5 and S6), demonstrating a rapid increase in the charge transfer resistance after the floating. This suggests possible electrode degradation, which may be attributed to the higher potential attained by the positive electrode (as observed during the voltage hold operation), or surface redox activities arising from electrode-electrolyte interaction. Another possible explanation for the capacitance loss could be electrolyte starvation or a reduction in the overall electrode surface area, limiting ions accessibility.^[49]

Considering that 20–30% decay of the initial capacitance is the acceptable range to measure the end life of a supercapacitor cell,^[46,52] we suggest that the true working potential of the cell lies between 2.2–2.4 V. These values corroborate the results presented in Figure 2(c), which suggest a potential limit 2.32 V. Moreover, it appears that the limitation of the positive electrode contributed to the supercapacitor's degradation before the negative electrode reached its actual potential as earlier suggested. Resolving this issue could potentially involve strategies such as mass balancing and the implementation of hybrid electrode approaches.

Upon establishing the operational limits, a symmetric supercapacitor cell was fabricated to evaluate its comprehensive performance, emphasizing on specific capacitance, energy, and power densities. Initially, a comparative study employing G-O as an electrode was conducted to establish the correlation between the combustion synthesis and the capacitive performance. Figures 3(a) and 3(b) depicts the GDC and the CV of r-GO versus G-O, at 2.4 V. As anticipated, G-O exhibited narrow voltage window and inferior capacitive behavior, recording specific capacitance values of 0.6, 0.8, and 1.1 F g⁻¹ at 2.2, 2.3, and 2.4 V, respectively. In contrast, r-GO exhibited notably enhanced performance, demonstrating specific capacitance values of 58, 59, and 61 F g⁻¹ at 2.2, 2.3, and 2.4 V, respectively. The enhanced performance for r-GO compared to G-O is likely attributed to its high surface area (522 m² g⁻¹) and the reduced surface functionalities. At lower current densities (ranging from 0.1–1 A g⁻¹), a noticeable dependency of specific capacitance on the applied potential was observed for r-GO based electrode (Figure 3(c)). However, this trend shifted at higher current densities (2–5 A g⁻¹), with r-GO displaying an equivalent capacitance value of approximately 32 F g⁻¹. The reduction in the observed capacitance may be attributed to the accelerated movement of ions within the cell at higher current densities. This constrains the time available for ions to be adsorbed onto the electrode surface.^[49] The power and energy performances of the cell at different current densities are presented in a Ragone plot (Figure S7). The result highlighted the suitability of the cell for applications requiring high current.

Figure 3(d) displays the CV measurements of the cell at different scan rates (from 10–1000 mV s⁻¹). The device maintained a nearly rectangular CV shape across all rates, indicating good capacitive behavior and outstanding rate capability.^[11] A more detailed analysis of the CV data at different scan rates allows for the qualitative distinction of the mechanism and quantitative assessment of the capacitive and non-capacitive contribution to the total current response. This characterization of the capacitive effect involves analyzing the CV data from different scan rates according to Eqs. (1) or (2):

$$i = av^b \quad (1)$$

$$\log(i) = \log(a) + b\log(v) \quad (2)$$

where the relationship between the peak current (i) and the scan rate (v) follows a power law, expressed by Eq.(1), and the b -values are derived from the gradient of $\log(i)$ vs $\log(v)$

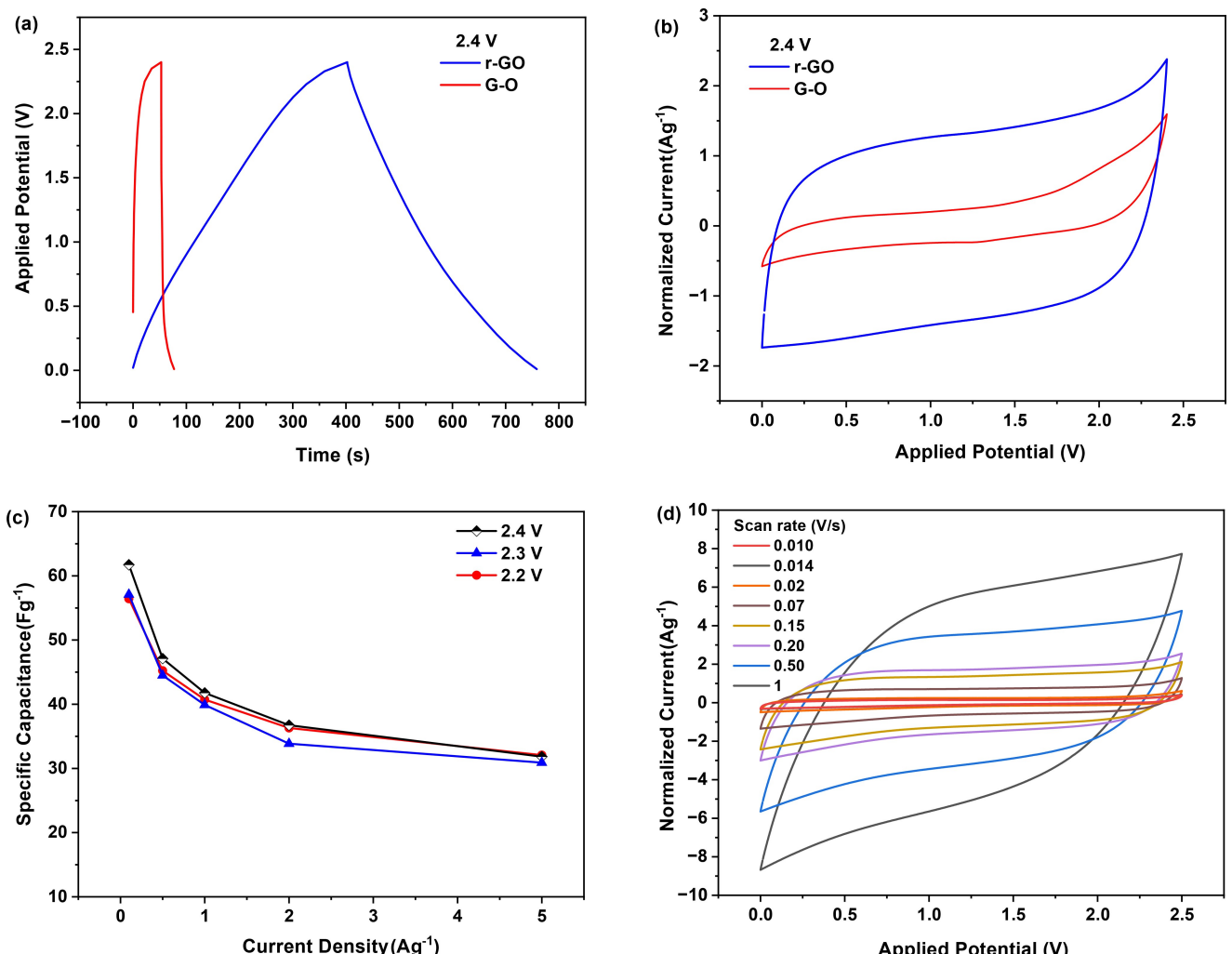


Figure 3. (a) GCD (0.1 A g^{-1}) curves of r-GO vs G-O at 2.4 V. (b) CV (100 mV s^{-1}) curves of r-GO vs G-O at 2.4 V. (c) Specific capacitance of r-GO at different current densities. (d) r-GO CV curves at different scan rates ($10\text{--}1000 \text{ mV s}^{-1}$).

according to Eq. (2).^[53,54] Conventionally, a b-value of "1" suggests current is solely attributed to the capacitive process, while a b-value of "0.5" indicates current is controlled by non-capacitive processes. Finally, a b-value between "0.5" and "1" implies the presence of both capacitive and non-capacitive processes.^[54,55]

Figure 4(a) depicts the obtained b-values at various potentials; the results suggest a discernible correlation between the b-values and the applied potential. At a lower potential of 1.5 V, the b-value stands at 0.843, indicating that the current primarily arises from the capacitive process with a minor contribution from non-capacitive processes. Within the potential range of 2.0 V to 2.4 V, the b-value falls within 0.83–0.70 respectively, still indicating the dominance of the capacitive process. However, beyond 2.4 V, the b-value shifted more towards indicating a non-capacitive process, primarily due to irreversible surface redox reactions and the electro-oxidation of stored hydrogen as the negative potential approaches its limit.^[16,17] This observation further suggests that the r-GO surface functionalities significantly impact the cell stability at high potentials due to possible

surface modification. Consequently, this causes cell degradation which limits the observable operational voltage window of the cell.^[2,48]

Another possible source contributing to the non-capacitive effect is the presence of supporting electrolytes (KCl in this context). Notably, this ME system relies on anionic surfactant (SDS) and inherently possesses conductivity without the need for supporting electrolytes. The key role of KCl (and other ionic salt) in the ME is primarily to enhance conductivity. This, in turn, lowers the cell's equivalent series resistance and enhances its power density.^[14] Hence, high chloride presence could potentially lead to non-capacitive contributions arising from the oxidation of chlorine. A comparison of the b-values between the blank ME and 0.1 M KCl ME is presented in Figure 4(b). At lower potentials, the obtained b-values showed a minimal difference, 0.85 for the blank ME and 0.84 for 0.1 M KCl ME. However, at higher potentials, the discrepancy in the b-values becomes evident. For instance, at 2.4 V, the b-values for blank ME and 0.1 M KCl ME are approximately 0.75 and 0.70, respectively. This observation underscores the non-capacitive

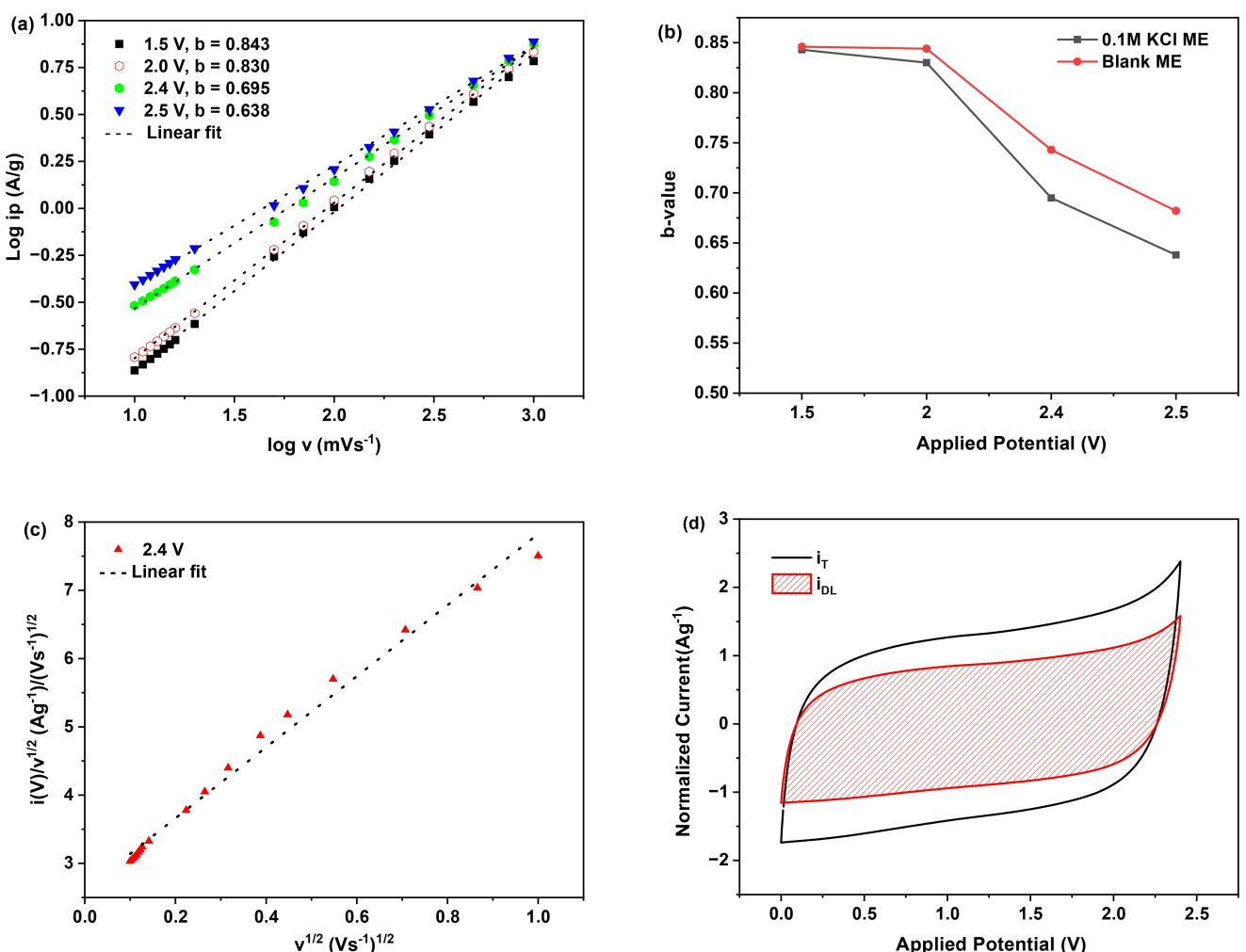


Figure 4. (a) Plot of $\log(i_p)$ versus $\log(v)$ used to obtain b-values at a different potential, with a scan rate of 10 to 1000 mVs⁻¹. (b) b-values for blank ME and 0.1 M KCl ME. (c) Plot of $(iv)/v^{1/2}$ versus $v^{1/2}$ used to calculate the constant k_1 and k_2 at 2.4 V, with scan rate from 10 to 1000 mVs⁻¹. (d) CV response (100 mVs⁻¹) for r-GO in 0.1 M KCl ME.

contribution originating from the KCl additive. It is plausible to suggest that, aside from the non-capacitive contribution from surface redox activities, the evolution of chlorine gas from the KCl additive serves as a significant contributing factor to the deterioration of the cell at high potential, hence this may have a profound influence on the voltage window.^[14] Investigating the impact of additives on ME performance in supercapacitors, and their influence on the electrode-electrolyte interface is ongoing research with our group.

It is now apparent that the charge storage mechanism of the supercapacitor device derived from r-GO and 0.1 M KCl ME involves both capacitive and non-capacitive processes. A detailed investigation of the CV at various scan rates allows for the quantitative deconvolution of capacitive and non-capacitive contributions to the current response. For supercapacitor devices where both mechanisms are observable, the peak current (at a particular potential) is the sum of the current from capacitive and non-capacitive processes, as illustrated in Eq. (3):

$$i(V) = k_1 v + k_2 v^{1/2} \quad (3)$$

$$\frac{i(V)}{v^{1/2}} = k_1 v^{1/2} + k_2 \quad (4)$$

Where k_1 and k_2 represent constant values associated with the capacitive and non-capacitive processes, respectively. By determining k_1 and k_2 values at a particular potential through the gradient (k_1) and the y-intercept (k_2) analysis of Eq. (4) above, it becomes possible to accurately quantify the current contribution associated with each process.^[53,54]

In Figure 4(c), the dependence of current on the scan rate was plotted according to Eq. (4). The linear trend observed in the graph allows us to determine the values of k_1 (from the gradient) and k_2 (from the y-intercept), enabling the quantification of capacitive and non-capacitive behaviors. The derived values of k_1 and k_2 , along with the relative capacitance contributions at different potentials, are presented in Table 1.

Figure 4(d) depicts the potential profile for the capacitive contribution (shaded area) at 2.4 V relative to the total

Table 1. k_1 and k_2 values (capacitive vs non-capacitive).

Potential [V]	k_1	k_2	R.C. ^[a] [%]
1.5	5.6804	1.0279	84.68
2.0	6.2136	1.1890	83.93
2.4	5.2032	2.6201	66.51
2.5	4.2775	3.6550	53.92

[a] Relative capacitance.

measured current (solid line) obtained from the CV response. Comparing the shaded area with the total stored charge revealed that the capacitive process contributed 84.7, 83.9, 66.5 and 53.9% at 1.5, 2.0, 2.4 and 2.5 V, respectively. Notably, a significantly higher contribution from the capacitive process was observed, particularly at the lower potential (1.5–2.2 V). These findings align with the obtained b values (Figure 4(a)) and those in Figure S4, which demonstrated a decrease in overall charge efficiencies and the voltage window due to an increase in the non-capacitive processes, resulting from r-GO surface functionalities.

Conclusions

Our research has demonstrated that MEs electrolytes can significantly improve the performance of graphene-based supercapacitors. By using a stable ME, we achieved a voltage window of 2.2–2.4 V, a notable enhancement compared to traditional aqueous electrolytes. This advancement is crucial for increasing the energy density of supercapacitors, addressing a key limitation when compared to batteries.

Our supercapacitor device showed a specific capacitance of 59 F g⁻¹ at 0.1 A g⁻¹ and 32 F g⁻¹ at 5 A g⁻¹, making it suitable for high-current applications. The charge storage primarily involves electric double-layer formation, with some contributions from non-capacitive processes related to electrode surface functionalities, electro-oxidation of hydrogen and the supporting electrolyte. We found that the stability of the supercapacitor decreases as non-capacitive effects become more significant, suggesting that the non-reversible pseudo-capacitive processes might contribute to the cell deterioration at higher potentials.

Ongoing research focuses on investigating the mechanism at the interface (EEI) and exploring the correlation between the structure of the ME electrolyte and electrochemical performance using neutron reflectometry (NR) and small-angle neutron scattering (SANS). These studies aim to provide deeper insights into the fundamental interactions and optimize the performance of these systems.

Our findings underscore the potential of ME electrolytes in energy storage, offering a wider voltage range while maintaining strong performance characteristics. This approach could serve as a practical and cost-effective alternative to more expensive and environmentally challenging organic or ionic liquid electrolytes.

Experimental

Graphene Synthesis

Commercially available graphitic oxide (Graphenea) synthesized using a modified Hummers method was utilized without any further treatments. The reduced graphene (r-GO) was produced by combusting the graphitic oxide (G-O) using a mixture of ammonium nitrate and urea, following a procedure reported by Satya et al.,^[42] with slight modifications. Initially, 300 mg of G-O was dispersed in 150 mL of deionized (DI) water and was subjected to ultrasonication for 1 h. Subsequently, 3.6 g (44.98 mmol) of ammonium nitrate (NH₄NO₂) and 2.7 g (44.6 mmol) of urea (CH₄N₂O) were added to the dispersed G-O solution. The resulting mixture was thoroughly stirred at 450 rpm and heated to 250°C on a hot plate, resulting in a dark colloidal solution. The temperature was held at 250°C until complete evaporation. The resultant product (r-GO) underwent extensive washing with 500 mL of DI water, followed by a wash with 50 mL of methanol, and finally, overnight drying under vacuum at 50°C.

Preparation of Microemulsion Electrolytes

Microemulsion samples were prepared using weight percentages. Cyclohexane and deionised water were used as the oil phase and water phase. The surfactant SDS and cosurfactant 1-butanol were mixed at a ratio of 1 to 2 w/w.

The preparation process involves weighing and mixing the appropriate components of the ME (82% water, 3.2% cyclohexane, 4.9% SDS, and 9.8% butanol) in a flask. This mixture underwent ultrasonication for approximately 15 min, followed by thorough stirring for 30 min until a clear, stable, single-phase ME solution was formed. For the ME with supporting electrolyte, a specific quantity of salt (KCl) was dissolved in the prepared ME solution. If a supporting electrolyte is added, the resulting ME electrolyte is labeled as "0.1 M KCl ME"; otherwise, it is referred to as "Blank ME". It is noteworthy that ME systems based on ionic surfactants like SDS exhibit conductivity without the need for additional supporting electrolytes.

Electrode Preparation

Electrode material slurry was prepared as reported in our previous paper.^[37] Briefly, an 8:1:1 ratio of graphene, binder (PolyVinylDene Fluoride, PVDF), and conductive carbon (super-P) was mixed with N-methyl-2-Pyrollidone (NMP) to form a viscous slurry, which was left magnetically stirring overnight to ensure good uniformity. The slurry was then coated on a graphite foil (0.127 mm, Ceramaterials) current collector by doctor blade followed by drying under vacuum at 120°C for 7 h. The specific loading of the slurry was ~1.5–2.0 mg cm⁻².

Electrochemical Measurement

CV and LSV measurements were conducted using a Swagelok T-junction cell to assess the electrochemical window of the electrolytes. This setup featured r-GO as the working electrode, a platinum rod as the counter electrode, and Ag/AgCl as the reference electrode. Cyclic voltammetry (CV) measurements of the full cell were performed in two electrode set-ups within a voltage range of 0–2.5 V. All cell assembly procedures were carried out under ambient laboratory conditions. A custom polyether ether ketone (PEEK) Swagelok-type cell was employed for the two-electrode measurements, while a glass microfiber (Whatman, grade GF/D)

soaked with 50–60 μL of the electrolyte served as the separator for all measurements. Prior to the CV measurements, it's important to highlight that there was no electrolyte degassing performed. The measurements were conducted using a Nova Metrohm Auto-lab 128 N potentiostat.

GCD measurements were carried out on a battery analyzer (Neware BTSCT-4008-164, MTI Corp). The GCD process involved an incremental increase in the cut-off potential, from 2 to 2.5 V. Gravimetric capacitance values of a single electrode (C_s) in Fg^{-1} were derived from the GCD discharge curve using the following Eq. (5).

$$C_s = \frac{2 \cdot I \cdot \Delta t_d}{\Delta V \cdot m} \quad (5)$$

where I signifies the discharge current (A), Δt_d denotes the discharge time (s), ΔV represents the IR-corrected cell potential, and m indicates the mass (g) of a single electrode. The energy density (E) of the supercapacitor cell was calculated using the formula in Eq. (6):

$$E = 0.5 \cdot \frac{C_s}{4} \cdot (\Delta V)^2 \cdot \frac{1}{3.6} \quad (6)$$

where E is in Wh kg^{-1} , C is the overall capacitance of the cell (F/g). The power density (P) was determined through the Eq. (7):

$$P = \frac{E}{t_d} \cdot \frac{1}{3600} \quad (7)$$

where P is in W kg^{-1} and t_d signifies the discharge duration (h). Coulombic (C_E) and energy (E_E) efficiencies were determined according to Eqs. (8) and (9):

$$C_E = \frac{t_d}{t_c} \cdot 100 \quad (8)$$

$$E_E = \frac{\int_{t_1}^{t_2} V(t_d) dt}{\int_{t_3}^{t_4} V(t_c) dt} \cdot 100 \quad (9)$$

where t_1 and t_2 are the minimum and the maximum discharge duration, t_3 and t_4 are the minimum and maximum charging duration, and t_c is the charging duration.

To assess the cell's stability, we conducted a floating (voltage hold) test utilizing the GCD Neware battery analyzer. Capacitance values obtained at various stages of the test were compared to determine the retained or lost capacitance. During the floating test, the cell voltage was maintained at 2.2 V, 2.3 V, and 2.4 V, in its charged state for a duration of 10 h.^[49] Subsequently, five GCD cycles were executed at a fixed current rate. This entire process was iterated five times, resulting in a cumulative floating duration of 50 h equivalent to 3.5 days of floating in total. Specific capacitance retention and equivalent series resistance (ESR) values were computed based on observations from the fifth discharge cycle.

Electrochemical impedance spectroscopy (EIS) measurements were carried out using a FRA32M module in a Nova Metrohm Auto-lab 128N potentiostat, across a frequency range from 0.1 to 100 kHz, with an amplitude set at 5 mV.

Characterisation

Transmission electron microscopy (TEM) samples underwent preparation via direct drop-casting of materials onto a 200-mesh holey carbon copper grid. Afterwards, TEM measurements were conducted utilizing JEOL JEM-F200 multi-purpose FEG-S/TEM, operating at an accelerating voltage of 200 kV. Raman spectra were obtained using a Renishaw inVia 2 Raman microscope at room temperature, employing 532 nm laser excitation. X-ray photoelectron spectroscopy (XPS) with a nonmonochromatic source was measured (Al K α ; 1486.6 eV, spot size; 10 mm, Mg anode) at a pass energy of 10 eV. XPS was used to determine the composition and chemical state of the components. The specific surface area was calculated from nitrogen adsorption/ desorption isotherm experiments recorded at 77 K (3Flex, Micromeritics). Before the analysis, the graphene like material was heated at 300 °C for a period of 15 h under vacuum in order to degas the contaminants physically adsorbed on the surface.

Supporting Information

Figure S1 detail the carbon distribution of reduced graphene oxide (r-GO) obtained from XPS spectra. Figure S2a present the C1s XPS spectra of GO whereas, S2b shows the N1s XPS spectra of r-GO. Figure S3 shows cyclic voltammograms, revealing the ESPW positive and negative limits of r-GO in microemulsions and other electrolytes. Figure S4 presents the Coulombic and energy efficiencies vs applied potential. Figures S5 and S6 present cyclic voltammetry, galvanostatic charge-discharge curves, and electrochemical impedance spectroscopy measurements before and after floating periods at various voltages, offering valuable insights into the supercapacitor's performance and stability under different conditions. Figure S7 presents the Ragone plot for power and energy densities at different current rates.

Acknowledgements

This work was supported by the University of Newcastle PhD Research Scholarship External (UNRSE). The authors also acknowledge the facilities, and the scientific and technical assistance of Microscopy Australia and the Australian National Fabrication Facility (ANFF) under the National Collaborative Research Infrastructure Strategy, at the South Australian Regional Facility, Flinders Microscopy and Microanalysis, Flinders University.

Conflict of Interests

The authors declare no conflict of interest.

Data Availability Statement

The data that support the findings of this study are available from the corresponding author upon reasonable request.

Keywords: supercapacitor • microemulsion electrolyte • graphene • voltage window • combustion synthesis

- [1] P. Sharma, T. Bhatti, *Energy Convers. Manage.* **2010**, *51*, 2901.
- [2] K. V. G. Raghavendra, R. Vinoth, K. Zeb, C. V. Muralee Gopi, S. Sambasivam, M. R. Kummara, I. M. Obaidat, H. J. Kim, *J. Energy Storage* **2020**, *31*, 101652.
- [3] A. González, E. Goikolea, J. A. Barrena, R. Mysyk, *Renewable Sustainable Energy Rev.* **2016**, *58*, 1189.
- [4] Poonam, K. Sharma, A. Arora, S. Tripathi, *J. Energy Storage* **2019**, *21*, 801.
- [5] L. L. Zhang, X. S. Zhao, *Chem. Soc. Rev.* **2009**, *38*, 2520.
- [6] A. Yu, V. Chabot, J. Zhang, *Electrochemical Supercapacitors for Energy Storage and Delivery: Fundamentals and Applications*, CRC Press, Boca Raton, 1 edition **2017**.
- [7] S. Zhang, N. Pan, *Adv. Energy Mater.* **2015**, *5*, 1401401.
- [8] F. Béguin, V. Presser, A. Balducci, E. Frackowiak, *Adv. Mater.* **2014**, *26*, 2219.
- [9] W. Yang, M. Ni, X. Ren, Y. Tian, N. Li, Y. Su, X. Zhang, *Curr. Opin. Colloid Interface Sci.* **2015**, *20*, 416.
- [10] Y. Wang, Z. Shi, Y. Huang, Y. Ma, C. Wang, M. Chen, Y. Chen, *J. Phys. Chem. C* **2009**, *113*, 13103.
- [11] M. D. Stoller, S. Park, Y. Zhu, J. An, R. S. Ruoff, *Nano Lett.* **2008**, *8*, 3498.
- [12] S. R. C. Vivekchand, C. S. Rout, K. S. Subrahmanyam, A. Govindaraj, C. N. R. Rao, *J. Chem. Sci.* **2008**, *120*, 9.
- [13] M. Shi, S. Kou, X. Yan, *ChemSusChem* **2014**, *7*, 3053.
- [14] C. Zhong, Y. Deng, W. Hu, J. Qiao, L. Zhang, J. Zhang, *Chem. Soc. Rev.* **2015**, *44*, 7484.
- [15] G. Wang, L. Zhang, J. Zhang, *Chem. Soc. Rev.* **2012**, *41*, 797.
- [16] L. Demarconnay, E. Raymundo-Piñero, F. Béguin, *Electrochem. Commun.* **2010**, *12*, 1275.
- [17] Q. Gao, L. Demarconnay, E. Raymundo-Piñero, F. Béguin, *Energy Environ. Sci.* **2012**, *5*, 9611.
- [18] K. Fic, G. Lota, M. Meller, E. Frackowiak, *Energy Environ. Sci.* **2012**, *5*, 5842.
- [19] S. Moulik, B. Paul, *Adv. Colloid Interface Sci.* **1998**, *78*, 99.
- [20] D. P. Acharya, P. G. Hartley, *Curr. Opin. Colloid Interface Sci.* **2012**, *17*, 274.
- [21] S. Qutubuddin, *Electrochemical Studies in Microemulsions*, in *Handbook of Microemulsion Science and Technology*, pages 651–678, CRC Press **2018**.
- [22] K. Chokshi, S. Qutubuddin, A. Hussam, *J. Colloid Interface Sci.* **1989**, *129*, 315.
- [23] H. M. Cheung, S. Qutubuddin, R. V. Edwards, J. A. J. Mann, *Langmuir* **1987**, *3*, 744.
- [24] R. A. Mackay, S. A. Myers, L. Bodalbhai, A. Brajter-Toth, *Anal. Chem.* **1990**, *62*, 1084, pMID: 2360716.
- [25] M. O. Iwunze, A. Sucheta, J. F. Rusling, *Anal. Chem.* **1990**, *62*, 644, pMID: 2316875.
- [26] J. F. Rusling, S. Schweizer, S. Zhang, G. N. Kamau, *Colloids and Surfaces A: Physicochemical and Engineering Aspects* **1994**, *88*, 41, a collection of papers presented at the 67th Colloid and Surface Science Symposium of the Colloid and Surface Science Division of the American Chemical Society.
- [27] J. Gao, J. F. Rusling, D.-I. Zhou, *J. Org. Chem.* **1996**, *61*, 5972.
- [28] A. Owlia, Z. Wang, J. F. Rusling, *J. Am. Chem. Soc.* **1989**, *111*, 5091.
- [29] Y. Makita, S. Uemura, N. Miyanari, T. Kotegawa, S. Kawano, T. Nishimi, M. Tominaga, K. Nishiyama, M. Kunitake, *Chem. Lett.* **2010**, *39*, 1152.
- [30] M. Kunitake, E. Kuraya, D. Kato, O. Niwa, T. Nishimi, *Curr. Opin. Colloid Interface Sci.* **2016**, *25*, 13.
- [31] J. Peng, N. M. Cantillo, K. M. Nelms, L. S. Roberts, G. Goenaga, A. Imel, B. A. Barth, M. Dadmun, L. Heroux, D. G. Hayes, et al., *ACS Appl. Mater. Interfaces* **2020**, *12*, 40213.
- [32] Y. Zheng, Álvaro Pérez Ramos, H. Wang, G. Álvarez, A. Ridruejo, J. Peng, *Mater. Today* **2023**, *34*, 101286.
- [33] S. Wei, Álvaro Pérez Ramos, J. Peng, Álvaro Ridruejo, P. Diao, *J. Energy Storage* **2024**, *75*, 109707.
- [34] J. Peng, Y. Xiao, A. Imel, B. A. Barth, N. M. Cantillo, K. M. Nelms, T. A. Zawodzinski, *Electrochim. Acta* **2021**, *393*, 139048.
- [35] J. Peng, N. M. Cantillo, Y. Xiao, K. M. Nelms, L. S. Roberts, G. Goenaga, A. Imel, B. A. Barth, M. Dadmun, D. G. Hayes, et al., *J. Electrochem. Soc.* **2021**, *168*, 080502.
- [36] K. Nakao, K. Noda, H. Hashimoto, M. Nakagawa, T. Nishimi, A. Ohira, Y. Sato, D. Kato, T. Kamata, O. Niwa, et al., *J. Colloid Interface Sci.* **2023**, *641*, 348.
- [37] F. R. Hughson, R. Borah, T. Nann, *Batteries & Supercaps* **2021**, *4*, 1122.
- [38] D. Liu, W. Peng, *New J. Chem.* **2023**, *47*, 16317.
- [39] G. Kamau, *Anal. Chim. Acta* **1988**, *207*, 1.
- [40] H. L. Poh, F. Šanek, A. Ambrosi, G. Zhao, Z. Sofer, M. Pumera, *Nanoscale* **2012**, *4*, 3515.
- [41] S. Pei, H.-M. Cheng, *Carbon* **2012**, *50*, 3210.
- [42] M. S. Kishore, P. Srimathi, S. Kumar, S. Addepalli, S. Swaminathan, V. Tilak, R. Colborn, *Bull. Mater. Sci.* **2013**, *36*, 67.
- [43] S. Biamino, C. Badini, *J. Eur. Ceram. Soc.* **2004**, *24*, 3021.
- [44] K. N. Kudin, B. Ozbas, H. C. Schniepp, R. K. Prud'homme, I. A. Aksay, R. Car, *Nano Lett.* **2008**, *8*, 36.
- [45] R. R. Salunkhe, Y. Lee, K. Chang, J. Li, P. Simon, J. Tang, N. L. Torad, C. Hu, Y. Yamauchi, *Chem. - Eur. J.* **2014**, *20*, 13838.
- [46] A. Laheäär, P. Przygocki, Q. Abbas, F. Béguin, *Electrochim. Commun.* **2015**, *60*, 21.
- [47] J. Piwek, A. Platek, E. Frackowiak, K. Fic, *J. Power Sources* **2019**, *438*, 227029.
- [48] H. Ang, H. T. Tan, Z. M. Luo, Y. Zhang, Y. Y. Guo, G. Guo, H. Zhang, Q. Yan, *Small* **2015**, *11*, 6278.
- [49] A. Bello, F. Barzegar, M. Madito, D. Momodu, A. Khaleed, T. Masikhwa, J. Dangbegnon, N. Manyala, *Electrochim. Acta* **2016**, *213*, 107.
- [50] D. Weingarth, H. Noh, A. Foelske-Schmitz, A. Wokaun, R. Kötz, *Electrochim. Acta* **2013**, *103*, 119.
- [51] P. Ratajczak, K. Jurewicz, P. Skowron, Q. Abbas, F. Béguin, *Electrochim. Acta* **2014**, *130*, 344.
- [52] K. Fic, A. Platek, J. Piwek, J. Menzel, A. Ślesiński, P. Bujewska, P. Galek, E. Frackowiak, *Energy Storage Mater.* **2019**, *22*, 1.
- [53] M. Forghani, S. W. Donne, *J. Electrochem. Soc.* **2018**, *165*, A664.
- [54] J. Wang, J. Polleux, J. Lim, B. Dunn, *J. Phys. Chem. C* **2007**, *111*, 14925.
- [55] K. Li, X. Wang, S. Li, P. Urbankowski, J. Li, Y. Xu, Y. Gogotsi, *Small* **2020**, *16*, 1906851.
- [56] M. D. Stoller, R. S. Ruoff, *Energy Environ. Sci.* **2010**, *3*, 1294.
- [57] J. W. Gittins, Y. Chen, S. Arnold, V. Augustyn, A. Balducci, T. Brousse, E. Frackowiak, P. Gómez-Romero, A. Kanwade, L. Köps, P. K. Jha, M. Meo, D. Pandey, L. Pang, V. Presser, M. Rapisarda, D. Rueda-García, S. Saeed, P. M. Shirage, A. Ślesiński, F. Soavi, J. Thomas, M.-M. Titirici, H. Wang, Z. Xu, A. Yu, M. Zhang, A. C. Forse, Interlaboratory Study Assessing the Analysis of Supercapacitor Electrochemistry Data, preprint, Chemistry **2023**.
- [58] T. S. Mathis, N. Kurra, X. Wang, D. Pinto, P. Simon, Y. Gogotsi, *Adv. Energy Mater.* **2019**, *9*, 1902007.

Manuscript received: May 6, 2024

Revised manuscript received: August 12, 2024

Version of record online: November 9, 2024